

Enhancing Tree Species Classification: Insights from YOLOv8 and Explainable AI Applied to TLS Point Cloud Projections

Adrian Straker^{1*}, Paul Magdon¹, Marco Zullich², Maximilian Freudenberg³,
Christoph Kleinn⁴, Johannes Breidenbach⁵, Stefano Puliti⁵, Nils Nölke⁴

¹ Faculty of Resource Management, University of Applied Sciences and Art (HAWK),
Göttingen, Büsgenweg 1a, 37077 Göttingen, Germany

² Department of Artificial Intelligence, University of Groningen, Nijenborgh 9, 9747 AG
Groningen, the Netherlands

³ Neural Data Science Group, University of Göttingen, Goldschmidtstraße 3, 37077
Göttingen, Germany

⁴ Forest Inventory and Remote Sensing, University of Göttingen, Faculty of Forest Sciences
and Forest Ecology, Burckhardt-Institute, Büsgenweg 5, 37077 Göttingen, Germany

⁵ Division of Forest and Forest Resources, National Forest Inventory, Norwegian Institute of
Bioeconomy Research (NIBIO), Høgskolveien 8, 1433 Ås, Norway

*Corresponding author: Adrian Straker; Email: adrian.straker@stud.uni-goettingen.de

Abstract

Classifying tree species has been a core research area in forest remote sensing for decades. New sensors and classification approaches like TLS and deep learning achieve state-of-the art accuracy but their decision processes remain unclear. Methods such as Finer-CAM (Class Activation Mapping) can highlight features in TLS projections that contribute to the classification of a target species, yet are uncommon in similar looking contrastive tree species. We propose a novel method linking Finer-CAM explanations to segments of TLS projections representing structural tree features to systematically evaluate which features drive species discrimination. Using TLS data from 2,445 trees across seven European tree species, we trained and validated five YOLOv8 models with cross-validation, reaching a mean accuracy of 96% (SD = 0.24%). Analysis of 630 saliency maps shows the models primarily rely on crown features in TLS projections for species classification. While this result is pronounced in *Silver Birch*, *European Beech*, *English oak*, and *Norway spruce*, stem features contribute more frequently to the differentiation of *European ash*, *Scots pine*, and *Douglas fir*. Particularly representations of finer branches contribute to the decisions of the models. The models consider those tree species similar to each other which a human expert would also regard as similar. Furthermore, our results highlight the need for an improved understanding of the decision processes of tree species classification models to help reveal data set and model limitations, biases, and to build confidence in model predictions.

Introduction

Tree species classification from remote sensing data has long been a challenging task. In addition to image-based data sets, 3D point clouds have been increasingly used in recent years. Terrestrial laser scanning (TLS) has emerged as a useful remote sensing tool for capturing detailed 3D information of individual trees. In recent years, deep learning models, particularly convolutional neural networks (CNNs), have become state-of-the-art for automatically classifying tree species using TLS data (Puliti et al. 2025). These approaches often leverage two-dimensional (2D) projections of TLS point clouds (Mizoguchi et al. 2017, Seidel et al. 2021, Allen et al. 2023, Puliti et al. 2025) or operate directly on the point cloud data itself (Liu et al. 2021, Chen et al. 2021, Liu et al. 2022, Puliti et al. 2025). Puliti et al. (2025) conducted a benchmark study and show that CNNs working on 2D projections generally outperform those applied directly to point clouds. The tree species classification CNNs working on 2D projections benchmarked in Puliti et al. (2025) are DetailView, YOLOv5, and SimpleView. These approaches achieved overall accuracies of 79.5 %, 77.9 % and 76.2 %, respectively. Whereas YOLOv5 scored highest by a margin of 0.1 % to the second-best approach (DetailView) when only applied to the TLS data of the FORSpecies20k data set (overall accuracy of 77.9%). The main use case of YOLO (Jocher et al. 2023) is to perform object detection and segmentation tasks in images and has been applied for individual tree crown detection/segmentation within aerial images (Sun et al. 2025), and grey-scale images of canopy height models from point cloud data (Straker et al. 2023). However, YOLO's classification head also allows for image-based supervised learning of classification tasks.

The fact that novel CNN-based tree species classification models trained on public individual tree point cloud benchmark data sets show high performance results may be interpreted as readiness for the operational use of these models on real life data. However, despite these recent advancements, little is known about how CNN-based tree species classification models using TLS data arrive at predictions, since often only standard evaluation metrics (e.g. recall, precision, F1-score and overall accuracy) are reported (e.g. Seidel et al. 2021, Allen et al. 2023, Puliti et al. 2025). These metrics focus on the performance outcome of a model but do not provide information on a model's decision process. Investigating the reasoning of a model for a final prediction is important to improve understanding of model limitations, potential biases, and to gain confidence in a model's predictions (Molnar 2025). Studies from other fields have shown that CNN-based models may learn shortcuts in the provided training data that correspond to data artifacts relevant features (e.g. Lapuschkin et al. 2019, Geirhos et al. 2020). This so-called shortcut learning leads to high model performance in experimental settings but hinders model generalizability when applied to real life data (Hinns & Martens 2025). Consequently, it is important to understand how those models come to their classification decision to create artifact-free TLS data sets. These can then in turn be used to further improve classification methods (e.g. Lines et al. 2022).

Explainable Artificial Intelligence (XAI) methods provide a valuable framework for understanding how CNN models make predictions. In the context of tree species classification, XAI methods can help reveal which structural features—such as crown shape, branching patterns, and stem morphology—contribute most to model decisions and thus show potential limitations of models and increase trust in model predictions. One widely used XAI approach is the construction of saliency maps (contribution maps), which provide a visualization by highlighting image regions most relevant to a model's prediction decision. In this regard Class Activation Mapping (CAM) developed by Zhou et al. (2016) generates a weighted sum of the outputs of global average pooling of each feature map at the last

layer to produce saliency maps. Based on this groundwork other approaches like Grad-CAM (Selvaraju et al. 2017), Grad-CAM++ (Chattopadhyay et al. 2018), EigenCAM (Muhammad et al. 2020), and Finer-CAM (Zhang et al. 2025) have been developed. While other CAM methods highlight all image regions important for a final class prediction, Finer-CAMs are more class discriminative since they only highlight features of the target class by suppressing features of the class visually most similar to the target class (Zhang et al. 2025). In the field of forest sciences, CAM have been used to understand tree species classification by CNNs using drone-based images (Onishi & Ise 2021, Ma et al. 2024), for the identification of bark features for tree species classification (Kim et al. 2022), for the detection of tree crowns in aerial images (Marvasti-Zadeh et al. 2023), and for the differentiation between leaves and wood in individual tree TLS point clouds (Han & Sánchez-Azofeifa 2022). In the context of tree species classification on TLS point clouds Xi et al. (2020) and Liu et al. (2022) used CAMs to visually interpret classification results. However, a comprehensive, systematic analysis of how convolutional neural networks perform tree-species classification from individual tree TLS point clouds — and which specific tree features drive their decisions — is still lacking.

Saliency maps can be considered local explanations, since they show visual explanations only for individual inputs. Interpretation of these is commonly conducted visually, which can be affected by cognitive biases (e.g. Mohseni et al. 2021; Bertrand et al. 2022). Consequently, manually analysing large amounts of saliency maps to find class specific repeating patterns is unsuitable. To compensate for these drawbacks Hinns & Martens (2025) have developed a method providing semi-global explanations by obtaining class specific patterns of saliency map explanations allowing for the recognition of shortcut learning. In their approach they associate saliency map explanations to image segments representing contextual information i.e image regions representing key features of the objects displayed. Similarly, we present an explanation framework in the context of tree species classification that allows for the association of saliency map explanations to segments representing structural tree features in 2D side-view projections of TLS point clouds.

We aim for insights into a YOLOv8-based tree species classification approach by the application of a novel framework linking Finer-CAM explanations to image segments representing structural tree features in 2D side-view projections of TLS point clouds. Specifically, our study aims to (1) systematically analyse which side-view projection segments associated with structural tree features contribute most to the decisions of YOLOv8, (2) determine whether these segments are used consistently across different species, and (3) assess the implications of these findings in regard to tree species classification models and TLS benchmark data sets.

Methods

Single tree TLS point clouds

We used a subset of the FORSpecies20k benchmark data set (Puliti et al. 2025) which consists of proximal laser scans (UAV-LS, MLS, TLS) of 19 962 individual trees of 33 tree species from Europe, Canada, Australia, and New Zealand. Being a compilation of already existing data sets, it shows strong class imbalance, variable tree height distributions among tree species classes, dissimilar representation of laser scanning types (UAV-LS, MLS, TLS), and data sources (research labs providing the data). To enhance the generalisability of the results by increasing the variability of data sources per class, a subset of the data set was created (Table 1). This subset included solely TLS data of tree species for which data is provided by a minimum of three different data sources.

This filtering resulted in a reduction to seven tree species. To compensate for the pronounced class imbalance, we reduced the number of samples for tree species classes with more than 1000 instances by randomly selecting 1000 trees per class. We randomly split the TLS point clouds for every species into training (90 %) and test data (10 %). We employed a cross-validation approach, where the training data was randomly shuffled and divided into five folds, with each fold serving once as the validation set during training and hyperparameter tuning. The test data was reserved exclusively for evaluating the performance of the final trained models.

Table 1. Subset of the FORSpecies20k (Puliti et al. 2025) used in this study.

Tree Species	No. of data sources	No. of individual tree terrestrial laser scans	No. of individual tree terrestrial laser scans in training folds / validation folds / test data set
<i>Silver birch (Betula pendula, Roth)</i>	5	171	123/30/18
<i>European beech (Fagus sylvatica, Linnaeus)</i>	3	1 000	720/180/100
<i>European ash (Fraxinus excelsior, Linnaeus)</i>	3	101	72/18/11
<i>Norway spruce (Picea abies, Linnaeus)</i>	6	533	384/95/54
<i>Scots pine (Pinus sylvestris, Linnaeus)</i>	7	1 000	720/180/100
<i>Douglas-fir (Pseudotsuga menziesii, Franco)</i>	3	355	256/63/36
<i>English oak (Quercus robur, Linnaeus)</i>	6	185	133/33/19

Orthographic 2D side-view projections of TLS point clouds

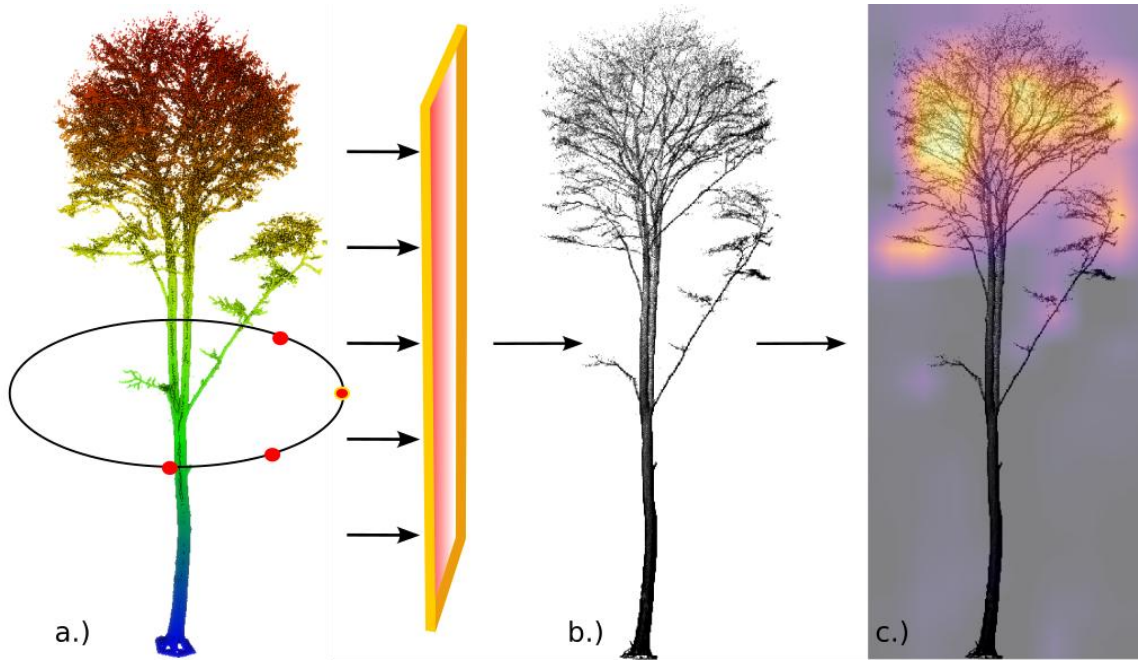


Figure 1 Workflow of the orthographic 2D projection of individual tree point clouds and saliency map generation. a.) Red circles indicate the positions from which the points are projected onto 2D planes. b.) From each position the points are orthographically projected onto a 2D raster to create a side-view projection. c.) saliency map projected onto a side-view image.

Similar to Zou et al. (2017) and Seidel et al. (2020) we used an orthographic projection approach to generate 2D side-view projections of TLS data of the training and test data sets (see Figure 1 a., b.). From here on, we refer to the 2D side-view projections of TLS data as side-view projections. In general, we followed a similar approach for the projection as presented in Puliti et al. (2025).

The points of some laser scans in the data set form regular point patterns, due to scanner properties. These regular point patterns, when associated with tree species, may hinder generalizability of the classification model and could lead to short cut learning since it may learn to differentiate tree species based on point distribution patterns. Consequently, we shifted all points by up to half a centimetre in random direction to confound regular point patterns.

To create the 2D side-view projections we projected all TLS points to a 2D plane which was rotated around the z -axis (which represents elevation) by angles α of 0° , 45° , 90° , and 135° in reference to north. Each plane is here be represented by two vectors u and v , where v points up (origin to tree top) and u spans the second direction of the plane. Computing the dot product of a given TLS point coordinate p with u and v yields the x and y coordinates within the plane:

$$u = [\cos(\alpha), \sin(\alpha), 0] \quad (1)$$

$$v = [0, 0, 1] \quad (2)$$

$$x = p \cdot u \quad (3)$$

$$y = p \cdot v \quad (4)$$

where α is the rotation angle and p is a TLS point. After each projection we created a raster with a pixel size adjusted to the point density of the point cloud. This step ensures that every tree point cloud is projected over the entire image canvas. We calculated the point density adjusted pixel size in metres (Δpx) as the theoretical space occupied by each point in the xy plane using the following equation:

$$\Delta px = \sqrt{(w \times h) \div n} \quad (5)$$

where h is the height of the tree on the z-axis of the point cloud, w is the maximum width of the tree on the y-axis of the point cloud and n is the number of points in the point cloud. We then aggregated the points along the x-axis of the point cloud by counting all points within each cell of the raster and stored the point count as pixel values. To mitigate the fact that extreme pixel values dominate the final grey-scale side-view projections, we log-transformed the pixel values. Finally, we stored each raster as a 640 pixels (px) \times 640 px grey-scale image.

YOLOv8 for tree species classification

Our approach builds on the tree species classification method presented in Puliti et al. (2025). While the original method used YOLOv5 on 2D orthographic projections of TLS point clouds, we used YOLOv8 (Jocher et al. 2023) here as it demonstrates superior performance compared to YOLOv5 on the COCO benchmark data set (Lin et al. 2014) and supports larger image sizes beyond 124 px \times 124 px. This enhancement allows for higher spatial resolution in side-view projections, improving the interpretability of classification results by enabling visualization of tree features with more details. YOLOv8 is characterised by a backbone and a classification head (Jocher et al. 2023). The backbone starts with two consecutive convolutional modules followed by four c2f blocks, of which the first three c2f blocks are each followed by a convolutional module. Each of the c2f blocks consists of a convolutional module that is followed by concatenated bottleneck modules (e.g. Heravi et al. 2018) that are followed by a convolutional module. In the first and last, and second and third c2f blocks three and six bottleneck modules are used, respectively. All convolutional modules in the backbone have a padding of 1, a stride of 2, and a kernel size of 3. The convolutional modules in the c2f modules have a padding of 0, a stride of 1 and a kernel size of 1. In all convolutional modules batch normalisation (Ioffe & Szegedy 2015) is performed and the SILU activation function (Elfwing et al. 2018) is applied. In the classification head a convolutional module is followed by a 2D adaptive average pooling layer, a dropout function (Hinton et al. 2012) and a linear transformation function.

The performance of a CNN is influenced by the training data it receives. Even minor changes in the training set or shifts in data distribution can result in unstable model predictions (Riley and Collins 2023). To mitigate this issue and enhance the reliability of our analysis, we evaluated the outputs of five independently trained YOLOv8 models. These models were trained using a five-fold cross-validation strategy, with each model utilizing different data subsets for training and validation. Additionally, we leveraged pre-trained weights (yolov8s-cls.pt, Jocher et al. 2023) originally trained on the COCO data set. During training we used a learning rate scheduler which is based on the “1cycle policy” described by Smith and Topin (2019) with an initial learning rate of 10^{-2} and minimum learning rate 10^{-4} . we reduced the initial learning rate during each test in steps of one tenth of the previously tested initial learning rate starting from 1×10^{-1} until a lower threshold of 1×10^{-4} was reached.

Based on these tests we selected an initial learning rate of 1×10^{-2} for the training of all models. We further set the batch size to 32 since it was the largest batch size suitable for the used hardware. We employed a stochastic gradient descent optimizer with weighted cross-entropy loss to compensate for class imbalance. We trained each model for 50 epochs and selected the weights that produced the highest overall accuracy on the validation fold without overfitting for further analysis.

For performance assessment we applied the trained models to the test data set in which each tree is represented by four side-view projections. To compute the final tree-wise species predictions we selected the class label with the highest average output logits among the class logits cast by a model of each tree's four side-view projections. We then calculated model- and class-wise F1-scores, recall and precision, and computed confusion matrices. To assess the overall performance of all models we calculated the macro averages of the model-wise F1-scores, Recall and Precision.

Finer-CAM description

Finer-CAM (Zhang et al. 2025) is a feature attribution method tailored for CNNs trained on image data and building upon Grad-CAM (Selvaraju et al. 2020). Its goal is to provide a value of *saliency*, usually normalized in the 0-1 range, to each of the input pixels of the image, according to its *importance* within determining the prediction of the model. It is an inherently *local* method, i.e., the saliency scores are only applicable to the single input being analysed, and does not generalize to global rules.

Finer-CAM generates the saliency map by fixing an intermediate layer l and storing the information provided by activations and gradients, as explained next. It additionally requires to define two classes the model is trained to recognize: (i) the category c , for which we want to generate the saliency scores, and (ii) a *contrastive category* c' , which acts as a *counterfactual* to the class c . In this sense, the Finer-CAM output will highlight pixels with positive attribution towards class c , but **not** towards class c' .

The gradients are calculated on the difference between the output logits $f(x)_c$ and $f(x)_{c'}$ and are computed with respect to the activations of the layer l . We formally indicate this as $\frac{\partial(f(x)_c - \gamma \cdot f(x)_{c'})}{\partial A^{(l)}}(x)_c$, with $A^{(l)}$ indicating the activations of layer l and γ is a comparison strength coefficient. The gradients are averaged on the spatial dimensions h, w , to produce a vector α . For a generic channel k ,

$$\alpha_k = \frac{1}{Z} \sum_{h,w} \frac{\partial(f(x)_c - \gamma \cdot f(x)_{c'})}{\partial A^{(l)}_{k,h,w}}, \quad (6)$$

where Z is the product of the spatial dimensions of the activation map. The vector α highlights the saliency, according to the gradients, of each of the channels within the map. It is further combined with the activations.

$$s_k = \alpha_k \cdot A^{(l)}_k, \quad (7)$$

where $A^{(l)}_k$ indicates the matrix of the activation map for channel k .

Finally, using the *ReLU* function, Finer-CAM suppresses negative values, retaining only *positive attributions*, i.e., indicating only those pixels who contribute positively towards class c (and not c'):

$$\text{FinerCAM}_k = \text{ReLU}(s_k). \quad (8)$$

Additionally, since usually the spatial dimensions of the activation map of layer l are smaller than the ones of the image, upsampling via bilinear interpolation is applied to the output of Finer-CAM to match the spatial dimension of the image, thus allowing the saliency map to be overlaid on top of the image (see Figure 2).

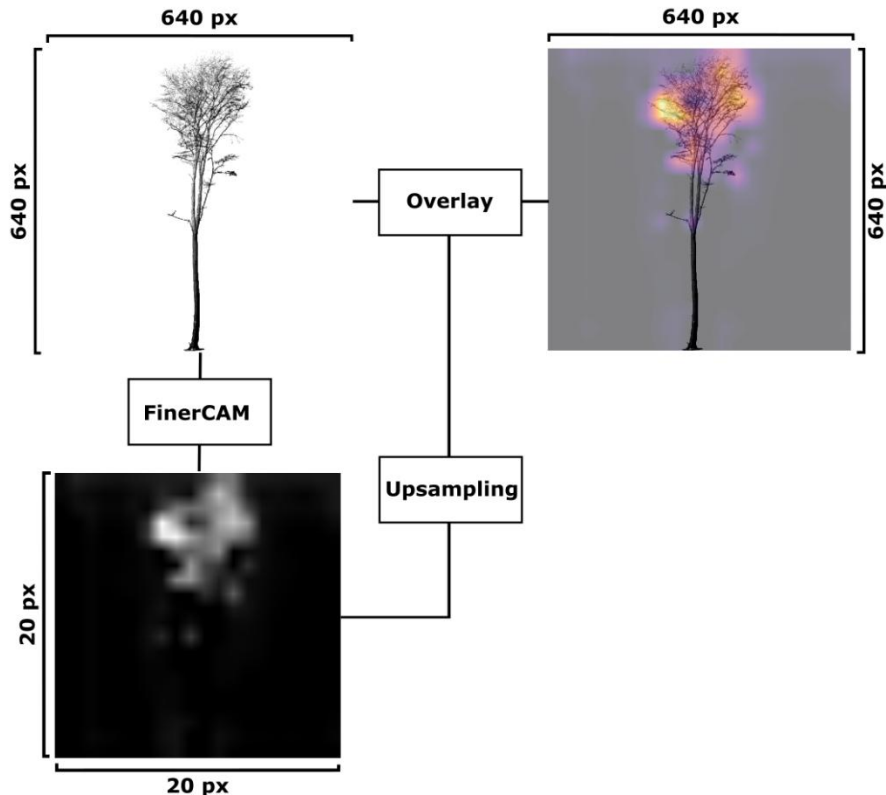


Figure 2 Upsampling of the output of Finer-CAM to the spatial dimension of the side-view projections and overlay of the upsampled saliency map on to a side-view projection.

Saliency map generation

In a Finer-CAM saliency map image features are highlighted that are used by a model to classify a target class, but are not common to contrastive classes most similar to the target class. Consequently, saliency maps are model and input specific. A model can use different image features among multiple images of a class and multiple models can produce different saliency maps for a given input image. To address these characteristics, we comprehensively analyse saliency maps of all five trained YOLOv8 models of the same selection of side-view projections of the test data set.

For the systematic analysis of saliency maps of all models we randomly selected 20 trees from the test data of each of Beech, Pine, Spruce, and Douglas-fir. The inclusion of more trees in our analysis would have increased evaluation time substantially and was hence dismissed.

Since the test data set includes less than 20 trees of *Birch*, *Ash*, and *Oak* we conducted no further sub-sampling. From each of the selected trees we randomly selected one of the four side-view projections when it was correctly classified by all five models. Consequently, we selected 20 side view projections of Beech, Pine, Spruce Douglas-fir, 18 side view projections of Birch, 19 side view projections of Oak, and 9 side view projections of Ash for further analysis.

For each one of the five YOLOv8 models we generated Finer-CAM saliency maps for each of the selected side-view projections using the Python library pytorch-grad-cam by Gildenblat (2021). We selected the last so-called c2f block in each model, which is the last layer before the classification layer, as the target layer for the saliency map generation. Finer-CAM allows for the aggregation of activation weights of multiple contrastive classes to produce more comprehensive saliency maps for a target class. We aggregated three contrastive classes most similar to a target class i.e. classes of which the output logits rank second, third and fourth after the output logit of the target class. similar to the procedure conducted by Zhang et al. (2025) who show this produces overall the best results. Further we set the comparison strength coefficient γ to 1. The comparison strength coefficient ranges between 0 to 1 while lower values and higher values produce coarser and finer saliency maps, respectively.

Heuristic integration of image partitioning and saliency mapping

To link recognizable tree features characterising the habitus of a tree in side-view projections with the predictions of the five models—and to reduce potential cognitive biases in saliency map interpretation (e.g. Mohseni et al. 2021; Bertrand et al. 2022)—we developed a heuristic approach to classify pixels from the saliency maps as related to tree, tree stem or tree crown. We further subdivided the tree crown into four sub-segments as shown in Figure 3.

Image partitioning

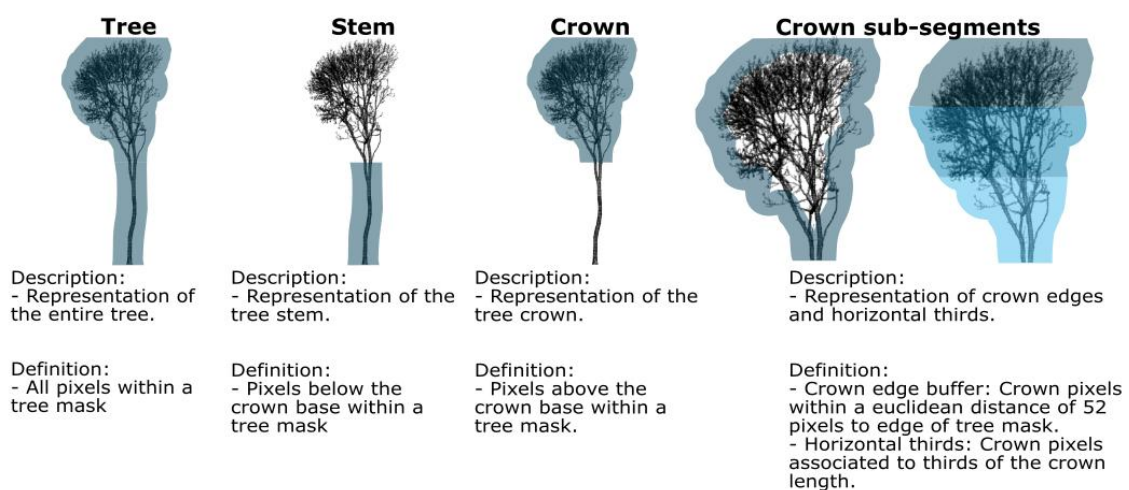


Figure 3 Descriptions and definitions of the image segments associated with tree features to which we attributed the saliency pixels.

To partition individual trees from side-view projections, we generated binary tree masks. In a first step we calculated tree contours by the application of a Gaussian blur filter (kernel size: 15×15 pixels) in which σ is computed from the kernel size as follows:

$$\sigma = 0.3 \cdot ((k - 1) \cdot 0.5 - 1) + 0.8 \quad (9)$$

where k is the one-dimensional kernel size. In a next step we applied binarization by setting pixel values to 255 and 0 when pixel values in the blurred images are higher or lower than a threshold of 0.0001, respectively. Finally, we extracted tree contours using the contour detection algorithm presented by Suzuki and Abe (1985).

The upsampling via interpolation is conducted with a scaling-factor of 32 during the generation of the saliency maps. This leads to a reduction in localization accuracy of the salient regions in the upscaled maps (see Figure 2). To mitigate the effects of the localization errors we created a buffer with a distance of 32 px around the tree contours for the generation of the tree masks. We consider pixels within the buffer as tree pixels.

To further partition into crown and stem regions, the height of the crown base was manually identified on each tree mask as the point where the stem transitions into multiple crown branches. In a straightforward scenario, pixels above the crown base were assigned to the crown, while those below were attributed to the stem. However, in instances where branches extended below the crown base, this method proved insufficient. To resolve this, the lowest crown pixel was also manually marked.

A path connecting the topmost and the lowest crown pixels was then computed using the *route_through_array* function from the scikit-image library (van der Walt et al. 2014). This algorithm determines the path of 1 pixel width that minimizes the cost between two points, where the cost of 1 is assigned to pixels within a tree, and the cost of 2 to pixels that fall outside of the tree. Prior to path detection, isolated pixel groups smaller than 64 pixels were removed to prevent noise interference. The resulting path approximates the stem's longitudinal axis. A buffer was then generated around this path, extending from the crown base to the lowest crown pixel, with the buffer width defined as the pixel width of a representative horizontal stem section (determined on a case-by-case basis). Tree pixels within this buffer and those below the lowest crown pixel were classified as the stem, while all remaining tree pixels were designated as the crown.

Recognizing the importance of crown morphology for species differentiation, the crown segment was further subdivided. The edges of the crown, which capture small branches, species-specific branching patterns, and terminal branch segments, were delineated by including all crown pixels within a Euclidean distance of 52 pixels from the edges of the tree masks. Moreover, inherent occlusions in TLS-derived point clouds often lead to under-representation of the crown tops, resulting in a negative correlation between tree height and point density. To evaluate the potential impact of these effects on species classification using YOLOv8, the crown was horizontally divided into three segments (base, middle, top), each corresponding to one-third of the crown's total height. Salient pixels were then assigned to their respective horizontal segments. Descriptions and definitions of the image segments are presented in Figure 3.

Evaluation of saliency maps

To analyse which tree species the models regard as similar to each other we tracked the three contrastive tree species most similar to the target (predicted) tree species i.e. species of which the output logits rank second, third and fourth after the output logit of the target species, of each saliency map. We then aggregated the contrastive tree species of all saliency maps of all five trained models and calculated the relative frequency of each contrastive species per target tree species.

We analysed all saliency maps to quantitatively assess the importance of the segmented features by attributing the salient pixels to the predefined image segments (i.e. tree, crown, stem, and crown sub-segments). This attribution allowed us to statistically evaluate the contribution of each segment to the model predictions. By combining detailed segmentation with pixel-level analysis of saliency maps, our approach quantitatively links recognizable tree features in the side-view projections to the decision-making process of the classification model while reducing reliance on potentially biased visual interpretations.

Since we are only interested in those regions of the side-view projection that have the highest contributions to class predictions, we counted pixels in the saliency maps as salient pixels when the pixel value was above a certain threshold which we computed per saliency map using Otsu's method (Otsu 1979). An example of a saliency map showing only salient pixel above a certain threshold defined by the application of Otsu's method is presented in the appendix (see Figure I). To ensure comparability between saliency maps and tree species we calculated the ratio of the number of salient pixels attributed to a segment and the number of salient pixels attributed to the segment one level above in the structural hierarchy. In Table 2, we define these ratios of salient pixels.

Table 2. Calculated ratios of the number of salient pixels (defined as pixels with a pixel value > a threshold computed by the application of Otsu's method) in each segment and abbreviations used in the following to refer to these.

Segment	Definitions of No. of salient pixels	Ratio of salient pixels
Tree	Nst = No. of salient pixels in tree segment $Nstot$ = No. of salient pixels in saliency map	$rNst = \frac{Nst}{Nstot}$
Stem	Nss = No. of salient pixels in stem segment	$rNss = \frac{Nss}{Nst}$
Crown	Nsc = No. of salient pixels in crown segment	$rNsc = \frac{Nsc}{Nst}$
Crown base	$Nscb$ = No. of salient pixels in crown base segment	$rNscb = \frac{Nscb}{Nsc}$
Crown middle	$Nscm$ = No. of salient pixels in crown middle segment	$rNscm = \frac{Nscm}{Nsc}$
Crown top	$Nsct$ = No. of salient pixels in crown top segment	$rNsct = \frac{Nsct}{Nsc}$
Crown edge buffer	$Nsce$ = No. of salient pixels in crown edge buffer segment	$nNsce = \frac{Nsce}{Nsc}$

To address the objectives 1.) systemic analysis of side-view projection segments associated to tree features and 2.) assess whether these segments are consistent across tree species we analysed the salient pixel association to segments jointly for all models. Here we aggregated the ratios of salient pixels for all segments at tree species level and over all tree species by calculating the arithmetic means and the standard deviations. On tree species level we further generated box plots of the ratios of salient pixels for all segments. To evaluate differences among tree species, we conducted statistical significance tests on the ratios of salient pixels of all segments. Normality of the data was assessed using the Shapiro-Wilk test, which revealed that the ratios of salient pixels in some segments were not normally distributed. Consequently, we employed the Dunn's test ($\alpha = 0.05$) for pairwise comparisons of the tree species. To mitigate the errors due to the performance of multiple significance tests (see Bender & Lange 2001) we used adjusted p-values applying the Holm-Bonferroni method (Holm 1979).

Results

To generate the following results, we selected the weights that produced the highest overall accuracy on the validation folds during training of the five YOLOv8 models. The highest overall accuracies during training were achieved after 40, 42, 44, 34, and 44 epochs for model 1, model 2, model 3, model 4, and model 5, respectively. On average the five trained models achieved an overall accuracy of 96 % ($SD = 0.24\%$), an F1-score of 92.5 % ($SD = 0.19\%$), a recall of 93.1 % ($SD = 0.26\%$), and a precision of 92.12 % ($SD = 0.44\%$) applied on the test data set. A confusion matrix summarizing the performance results of all models is presented in Figure 4. The confusion matrix of each individual model is presented in the appendix (see Figure II).

		Precision %							Recall %
		87.6	97.4	83.3	91.6	99.2	98.0	92.9	
True	Birch	85	0	4	0	0	1	0	94.4
	Beech	5	492	0	3	0	0	0	98.4
	Ash	2	6	45	2	0	0	0	81.1
	Oak	0	2	5	88	0	0	0	92.6
	Pine	0	0	0	0	498	0	2	99.6
	Spruce	5	5	4	1	0	244	11	90.4
	Douglas-fir	0	0	0	2	4	4	170	94.4
		Broadleafes				Coniferous			
		Birch	Beech	Ash	Oak	Pine	Spruce	Douglas-fir	

Figure 4: Confusion matrix, class-wise precision and recall summarizing the performance of all five trained YOLOv8 models applied to the test data set.

Highlighted regions in the analysed saliency maps represent features in the side-view projections which contribute most to the classification of a target tree species but are uncommon for three contrastive tree species most similar to the target species i.e. classes of which the output logits rank second, third and fourth after the output logit of the target class. Example saliency maps of all models generated for the same side-view projections of broad leafed and coniferous tree species are presented in Figure 5 and Figure 6, respectively. These examples demonstrate that for every presented side-view projection all models focus on similar image regions. This is less apparent for the example of *Spruce* for which indeed image regions in the crown contribute most across all models, but the location of salient regions in the crowns differ across the models. Contrary, for the presented side-view projection of *Ash* all models of this example tree focus on the same part of the stem, which represents a bent in the stem. On average 64.4 % of the analysed saliency maps of *Ash* of all models

bends in stems contribute to the classification of Ash. In the examples of *Birch*, *Beech*, *Spruce*, *Pine*, *Douglas-fir*, and *Oak*, image regions representing branches contribute most to the decisions of all models. For *Pine* and *Douglas-fir* these branches are attached to the stems, whereas for the rest the models focus on branches in the tree crowns. The observation that the five models use similar regions in the side-view projections to discriminate tree species is further supported by analysis results provided in the appendix in which we present a table (Table a) of the model-wise average ratios of salient pixels aggregated to segments associated to structural tree features. Additional examples of saliency maps of all tree species of model 1 are presented in Figure 7 and Figure 8.

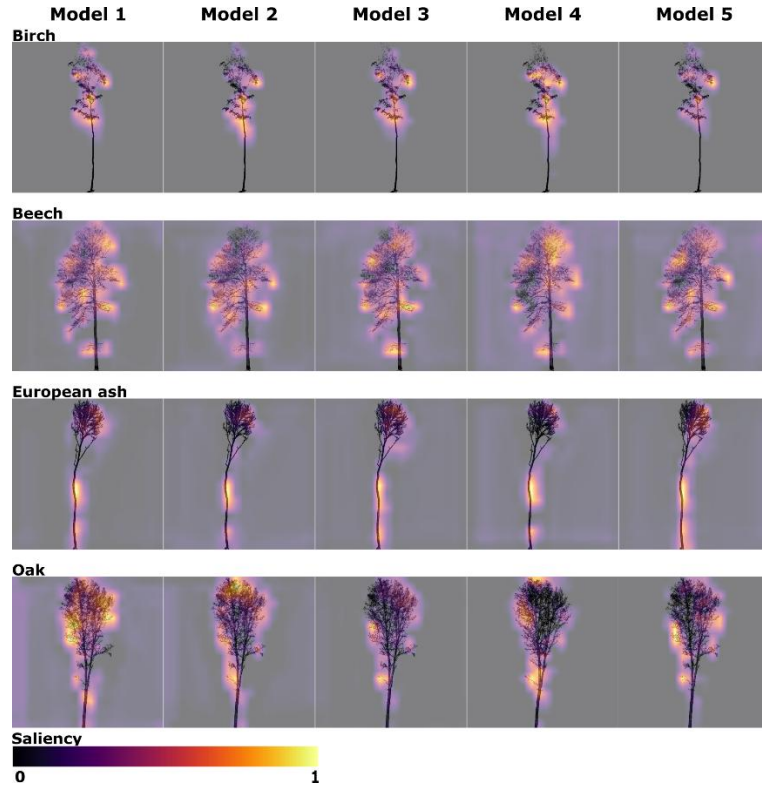


Figure 5 Example saliency maps of all five YOLOv8 models of the same side-view projections of *Birch*, *Beech*, *Ash*, and *Oak* overlayed with the TLS side-view projections. Layer activations for a species class are depicted in a colour gradient from purple to yellow, where yellow and purple correspond to the regions with high and low importance attached to them, respectively.

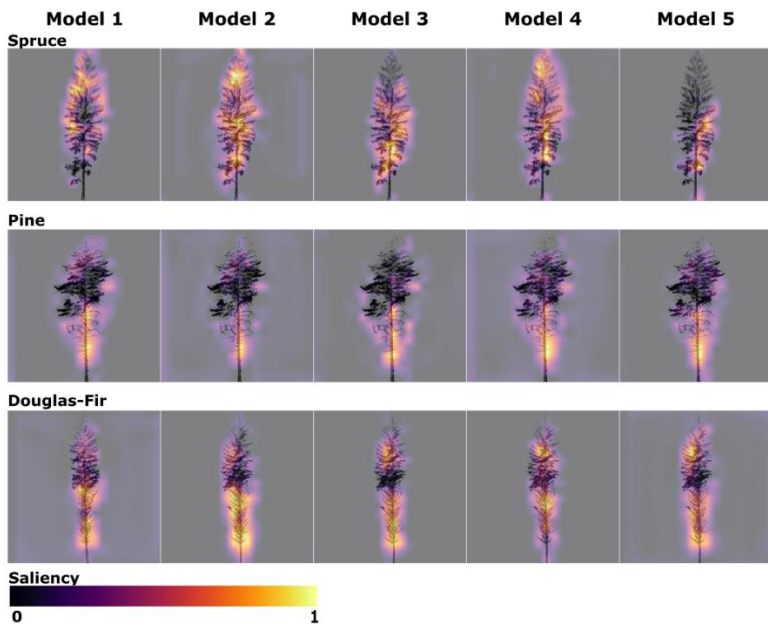


Figure 6 Example saliency maps of all five YOLOv8 models of the same side-view projections of *Spruce*, *Pine*, and *Douglas-fir* overlaid with the TLS side-view projections. Layer activations for a species class are depicted in a colour gradient from purple to yellow, where yellow and purple correspond to the regions with the high and low contribution for the decision of a model, respectively.

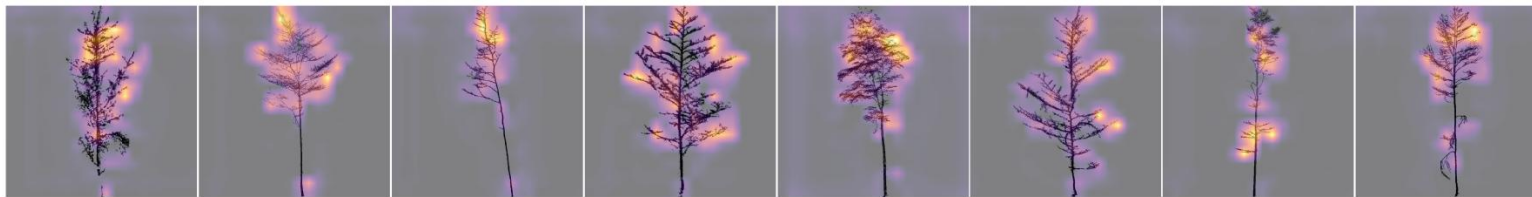
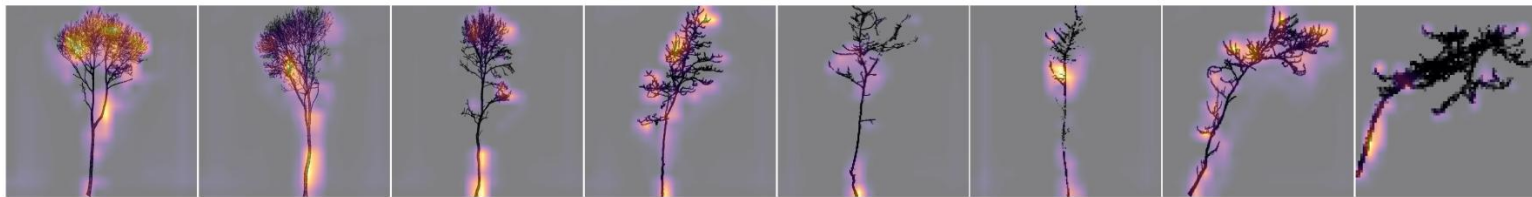
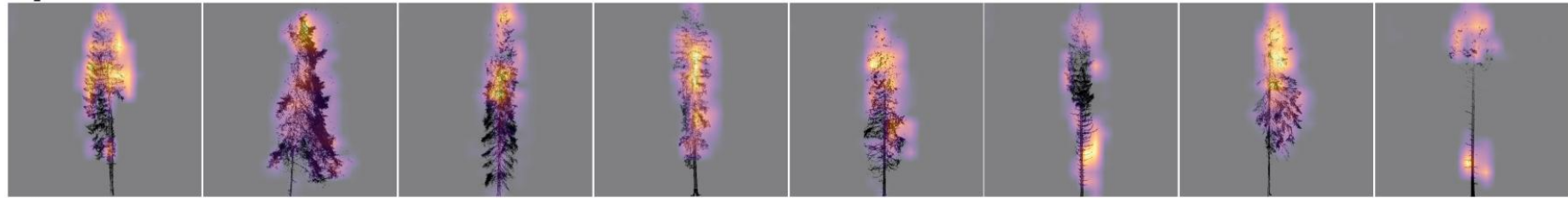
Birch**Beech****Ash****Oak****Saliency**

Figure 7 Example saliency maps of model 1 of Birch, Beech, Ash, and Oak overlaid with the TLS side-view projections. Layer activations for a species class are depicted in a colour gradient from purple to yellow, where yellow corresponds to pixels with high importance attached to them. Pixels with no importance attached to them are depicted in purple.

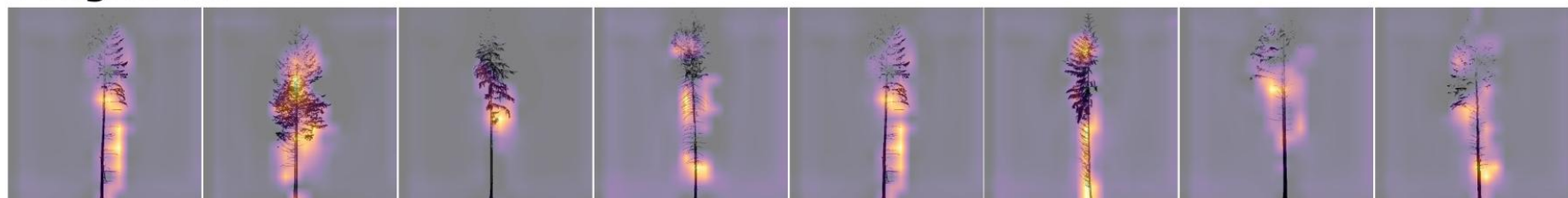
Spruce



Pine



Douglas-Fir



Saliency



Figure 8 Example saliency maps of model 1 of Spruce, Pine, and Douglas-fir overlaid with the TLS side-view projections. Layer activations for a species class are depicted in a colour gradient from purple to yellow, where yellow corresponds to pixels with high importance attached to them. Pixels with no importance attached to them are depicted in purple.

The aggregation of the contrastive tree species of all saliency maps of all five trained models is presented in Figure 9. In general, broadleafed tree species have the highest share among the first two most similar contrastive species of all boradleafed species. For *Spruce* and *Douglas-fir* coniferous tree species have the highest share among the first two similar contrastive species. Contrary to this, for *Birch* has the highest share among the first most similar contrastive tree species of *Pine*. While coniferous tree species have only the highest share among the second and third most similar contrastive tree species of *Pine*.

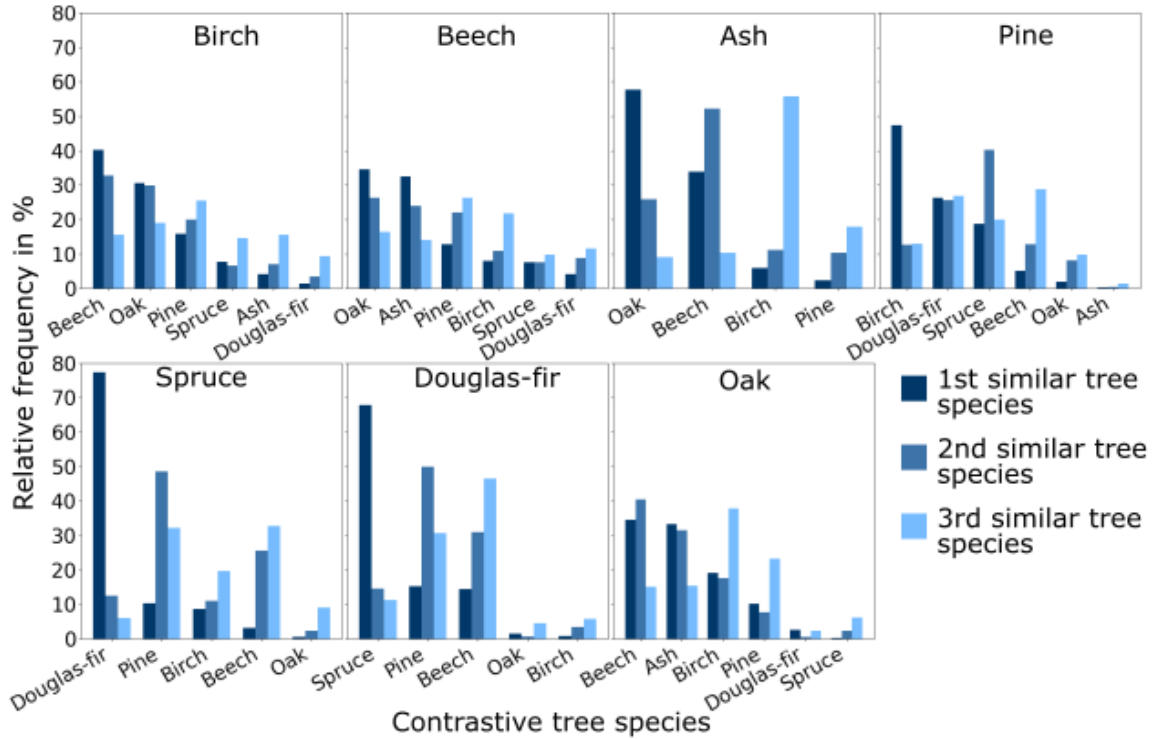


Figure 9 Frequency of first, second, and third most similar contrastive species per target tree species aggregated over all saliency maps and models.

To evaluate the contribution of regions in the side-view projections associated with structural tree features i.e stem, crown, crown sub segments, to the decisions of all five YOLOv8 models over all tree species, we present the segment-wise arithmetic means and standard deviations of the aggregated ratios of salient pixels of all tree species and models in Figure 10. On average most salient pixels are in the crown segments (68.6 %). Among the crown sub-segments (crown top, crown middle, crown base) the average ratio of salient pixels is lowest in the crown top segments. On average nearly as many salient pixels of the crown segments are located at the edges of the crown as within crown centres (average ratio of salient pixels in crown edge buffer = 48.1 %).

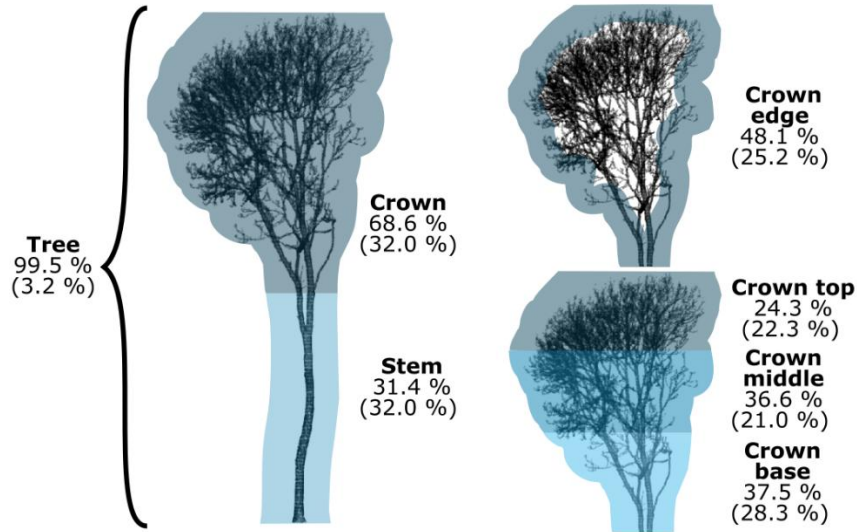


Figure 10 Segment-wise arithmetic means and standard deviations (in brackets) of the ratios of salient pixels associated to image segments over all tree species and aggregated over all five YOLOv8 models.

To assess whether the five YOLOv8 models use similar side-view projection, regions associated with structural tree features across all tree species to discriminate tree species we present tree species comparisons of the aggregated ratios of salient pixels in the tree, crown, and stem segments averaged across the results of all five YOLOv8 models in Figure 11. Multiple pairwise comparisons using the Dunn's test with adjusted p-values using the Holm-Bonferroni method show significant differences of the ratios of salient pixels in the stem and crown segments between *Ash*, *Pine*, and *Douglas-fir* and the other tree species. The ratios of salient pixels in the stem segments of *Ash*, *Spruce*, and *Douglas-fir* are significantly higher than of the other tree species.

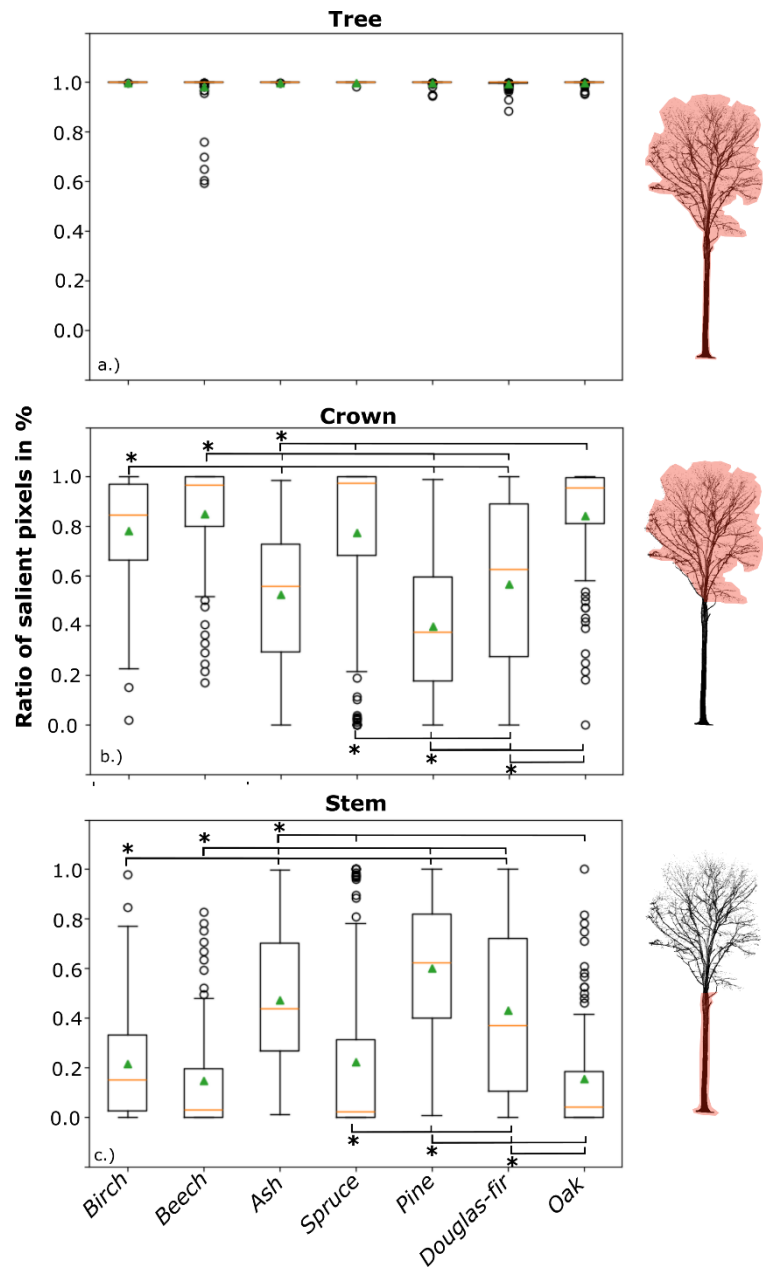


Figure 11. Species-wise box plots of the ratios of salient pixels of saliency maps of five YOLOv8 models. Saliency maps were generated for a random selection of 128 side-view projections of seven tree species of the test data set. The ratios of salient pixels are associated to tree a.), crown b.) and stem c.) segments. Horizontal lines in boxes represent the medians, green triangles the arithmetic means, the box boundaries the first and third quartile, the whiskers are the first quartile minus 1.5 times the interquartile range and the third quartile plus 1.5 times the interquartile range. The circles show outliers. Brackets below and above the box plots in b.) and c.) indicate significant ($\alpha = 0,05$) differences after p-value adjustment using the Holm-Bonferroni method between species of interest (marked with asterisk) and other species.

The tree species comparisons of the ratios of the salient pixels in the crown sub-segments crown (crown base, crown middle, crown top, crown edge buffer) averaged across the results of all five YOLOv8 models are presented in Figure 12. Here it shows that the average ratios of salient pixels in the crown middle segments are similar among all tree species except for *Spruce*, which has significantly the highest average ratio of salient pixels in the crown middle segment.

Comparing the average ratios of salient pixels of the crown top segments with the ratio of salient pixels of the crown base segments of *Birch*, *Beech*, *Pine*, and *Douglas-fir* it is observable that while the average ratios of the salient pixels of the crown top segments are low, the average ratios of the salient pixels of the crown base segments are high, and vice versa.

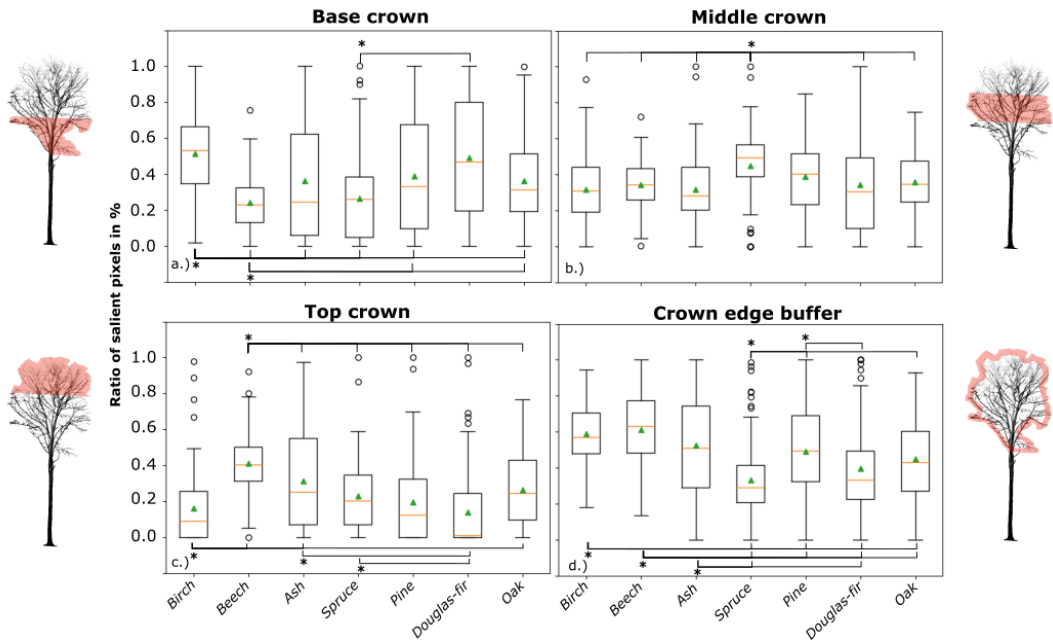


Figure 12 Species-wise box plots of the ratios of salient pixels of saliency maps of five YOLOv8 models. Saliency maps were generated for a random selection of 128 side-view projections of seven tree species of the test data set. The ratios of salient pixels are associated to crown sub-segments crown base a.), crown middle b.), crown top c.), and crown edge buffer d.), segments. Horizontal lines in boxes represent the medians, green triangles the arithmetic means, the box boundaries the first and third quartile, the whiskers are the first quartile minus 1.5 times the interquartile range and the third quartile plus 1.5 times the interquartile range. The circles show outliers. Brackets below and above the box plots in b.) and c.) indicate significant (alpha = 0,05) differences after p-value adjustment using the Holm-Bonferroni method between species of interest (marked with asterisk) and other species.

Discussion

Our results suggest that side-view projections of TLS scans describe the habitus of trees, in the sense of tree structure, which then is used by YOLOv8 models to discriminate tree species. On average all five independently trained YOLOv8 models use areas of the side-view projections representing the trees (average ratio of salient pixels of the tree segment = 99.5 %) to discriminate tree species. This result confirms an expected behavior of the models, that indeed tree features in the side-view projections contribute to the decisions of the models rather than i.e. image backgrounds, for which a contribution would be difficult to explain. Our results show that crown features contribute most to the decisions of the models to differentiate tree species (see Figure 10), since the average ratio of salient pixels in the crown segments aggregated over all models and tree species is higher than the average ratio of salient pixels in the stem segments. The pronounced focus on crown features can be particularly observed for *Birch*, *Beech*, *Spruce*, and *Oak*. By visually interpreting the saliency map examples of these tree species it becomes apparent, that individual branches of higher orders (i.e. finer branches) and arrangements of these branches seem to contribute most to the decisions of the models to discriminate these species from their most similar tree species.

This can be interpreted as the capability of the models to learn species specific branching patterns of finer branches rather than the shape of the tree crowns to differentiate tree species, which is reasonable from a human expert's position. For *Birch*, *Beech*, and *Oak* the average ratios of salient pixels in the crown edge buffer segments are around 50 %. Since the edges of the tree crowns mostly show finer branches, this result provides additional support to the conclusion that the models use species specific branching patterns of finer branches for classification of these tree species. More finer branches in the edges of the crowns are visible than in the center of the crown, because of an increased possibility of overlap of branches towards the center of the crowns which is an inherent characteristic of the side-view projections. Our results further indicate that among *Birch*, *Beech*, *Spruce*, and *Oak* the crown base segments and the crown top segments contribute most to the decisions of the models in the classification of *Birch* and *Beech*, respectively. Under visual interpretation of the saliency maps of both tree species it is observable that salient regions are mostly located at finer branches. For *Birch* these finer branches and their branching patterns are more distinctively visible in the base towards the edges of the crown than in the top of the tree crowns because the tree tops are often underrepresented in the side-view projections due to occlusion of lower branches. Contrary, many analysed side-view projections of *Beech* have high spatial resolutions leading to detailed representations of the tree crowns. Consequently, in those instances small branches are visible across the entire length of the crowns even in the top of the crown and particularly in the edges of the tree crowns. However, also in instances of *Beech* with low spatial resolutions in which crowns are depicted in low detail, regions in the crowns depicting branches contribute most to the model decisions. These observations indicate that the models learn features of branches specific to *Birch* and *Beech* independent to spatial resolution.

While over all models the average ratios of salient pixels in crown segments are higher than the average ratios of salient pixels in the stem segments for nearly all tree species (except *Pine*) our results indicate that stem features -besides crown features- contribute to the decisions of the models. On average the models use stem features more often to discriminate *Ash*, *Pine*, and *Douglas-fir* from their most similar contrastive species than to differentiate the other tree species. For *Pine* and *Douglas-fir* the models predominantly focus on branches attached to the stem (see Figure 6 and Figure 8). Both species retain dead branches at the stems since self-pruning rates are low. This shows that models learn stem features specific to *Douglas-fir* and *Pine*. On average all models focus in 64.4 % of the side-view projections of *Ash* on bends of stems to discriminate *Ash* from its most similar tree species explaining the high contribution of stem segments to the decision of the models (see Figure 5 and Figure 7). Bends in stems are expected in any tree species as a consequence of a tree's natural growth and a reaction to external factors like changes in light conditions, wind, and snow. Consequently, the occurrence of bends in stems can in general not be seen as specific only to *Ashes*. This result can be interpreted in a way that the models learn a feature of the data set (bends in stems are common for *Ash* in the data but not for its most similar species) rather than structural features specific to *Ash* potentially leading to a high failure rate, when the models are applied to external data. This could be tested in future research by applying the trained models to instances of other tree species in which stem bends similar to the ones observed for *Ash* are present.

The evaluation of the aggregation of contrastive species (see Figure 9) reveal similarities between which tree species are regarded as similar by the models and which tree species a human expert looking at the tree habitus would regard as similar. The models regard *Spruce* and *Douglas-fir* most frequent as most similar to each other, while *Pine* is regarded most often as the second most similar

species to both. From a human expert perspective -while all are coniferous- only Spruce and Douglas-fir show a similar habitus. Broadleafed species are regarded most frequently as the third most similar species to *Spruce* and *Douglas-fir*, which is something a human expert would not agree upon when looking at the habitus, but which is expectable since in total we only consider three coniferous species. Birch is most frequently regarded as most similar to *Pine*, whereas the other coniferous species are most often seen as second and third similar species. The habitus of *Pine* and *Birch* are similar which, as light-demanding species, have rather open crowns. Only broadleafed tree species are among the most frequent most, second and third similar species of *Ash*. Whereas *Pine* is the most frequent third similar tree species to *Oak* and *Beech*, while the most and second frequent similar tree species are broadleafed species. From the perspective of a human expert the habitus of *Pine* can be similar to broadleafed species.

By and large our results reveal similarities and differences among the studied tree species that a human expert looking only at the habitus of trees would potentially also ascertain. However, the agreement between salient regions and regions in the side-projections used by human experts for tree species classification is not further assessed here but would be a suitable topic for future research. Further it may be of interest to study the performance of a classification model solely trained on detailed views of stem and crown regions. If this model shows a performance similar to the one described in this study, it would mean that only fractions of the TLS point cloud data are needed for tree species classification resulting in reduced storage capacities needed. A method that uses detailed representations of stems in addition to side-view and top-view projections of point clouds called DetailView is benchmarked in Puliti et al. (2025) and performs best among all tested approaches.

Our results should not be interpreted as an absolute statement on the global contribution of tree features for tree species classification but rather as an indication of which features are most accessible to the models under the chosen study design. The occurrence of visible tree features in side-view projections is linked to the design of these. Consequently, the models can only learn tree features that are present in the side-view projections. This is also affected by limitations imposed by the data set which show in unequal tree size distributions across tree species. Since we projected all individual tree point clouds to the same canvas size tree size is directly translated into varying spatial resolutions of the images. Thus, features of smaller trees are likely to be represented in finer detail than for larger trees, possibly affecting which tree features are learned by the models. Accounting for these potential affects was infeasible because of the relatively low number of individual tree point clouds for some tree species included in the data set. This data set limitation further highlights the need for comprehensive public TLS data sets consisting of trees in various developmental stages from different regions and for which TLS point clouds are collected with various scanners from different working groups. The effects of differences in spatial resolutions of the side-view projections on the analysis of salient regions may be amplified by the limited number of saliency maps (maximum 20 per tree species) analysed, which may hinder comparability of the tree species. However, our results show that model decisions are driven by species specific features present in the side-view projections rather than by random effects. This further renders our proposed approach feasible linking salient pixels to image segments related to structural tree features. The results may be negatively affected by errors introduced during the application of image partitioning (generation of segments) and the allocation of salient pixels to image segments. Firstly, the visual determination can be regarded as subjective, which could result in potential inaccuracies during the visual determination of the crown base used to delineate crown and stem segments. This might have influenced the allocation of salient pixels

between these segments. However, this source of uncertainty is considered minor given that the visual determinations were independently verified. Secondly, discrepancies introduced during the tree contour generation process may also have impacted the analysis results in a way that salient pixels may be wrongly associated to image segments. During the generation of tree contours we applied a gaussian blur filter followed by image binarization. In instances in which the tree crown tops are under-represented in the side-view projections due to TLS inherent point cloud characteristics (reduced point density in tree tops), this step leads to tree contours cutting through tree top representations in the side-view projections.

All trained YOLOv8 models show high classification accuracies across all tree species. However, although we aimed to increase generalisability by including only tree species for which TLS data is provided by at least three data sources, the classification accuracies might be optimistic due to spatial autocorrelation within the data sources. The models most frequently confuse coniferous with other coniferous and broadleafed with other broadleafed species, which is relatable as a human expert looking at the habitus of species. This is generally in accordance with our assessment of the contrastive species of each target species. However, the tree species a tree species is most often confused with is only for Spruce and Douglas-fir the one the models regard to be most the most similar most frequently.

It is difficult to directly compare our results to other studies investigating saliency maps in the context of tree species classification using individual tree TLS point clouds, since these studies focus on mostly different tree species, only present saliency maps for some example instances, and analyse them only visually (e.g. Xi et al. 2020, Liu et al. 2022). Visual interpretations come with human biases, which effects on the interpretation results of XAI are discussed in the literature (Mohseni et al. 2021, Bertrand et al. 2022). Additionally, these studies applied tree species classification models performing directly on the individual tree TLS point clouds and present saliency maps projected onto point clouds or so-called critical points that contribute most to the learned features in the used CNNs. However, the results presented by Liu et al. (2022), which show critical points mostly in the tree crowns, appear to support our results that tree crown features contribute to tree species classification. Xi et al. (2020) conclude that crown features contributed to the classification of four (*Cottonwood, Maple, Norway spruce, White Spruce*) of their tested nine tree species. For the other tested tree species (*Lodgepole Pine, Red Pine, Scots pine, Birch, and Aspen*), the stem appeared to be more important for a correct classification, which is also in line with our results showing that contribution of stem and crown features are high for Scots pine and Norway spruce, respectively. In regard to birch their results differ from ours, which is difficult to interpret based on the results presented by Xi et al. (2020).

Our results indicate minimum data requirements needed for the use of the presented YOLOv8-based approach and highlight the need for explanations of model decisions in the field of tree species classification using TLS point cloud. In regard to minimum data requirements our results show that point densities of the used TLS point clouds must be high enough so that individual branches or branch arrangements either in the tree crowns or at the stems are distinguishable in the side-view projections, since they contribute most to the decisions of the models. Further, our analysis results of *Ash* may hint towards a potential limitation in the sense that models learn data set artifacts rather than actual tree features (i.e. bent stems were predominantly a feature specific to *Ash*). Although our results do not allow for a final conclusion in this regard, they highlight the need for future research that i.) quantitatively assesses the feature contributions for the decisions of other CNN-based tree

species classification models, ii.) investigates the occurrence of data set artifacts of publicly available TLS data sets and their effects on the decision of CNN for tree species classification, and iii.) analyses the generalizability of CNN-based tree species classification models trained on public benchmark data sets by application on fully independent test data sets. We argue that findings in these fields have the potential to create sophisticated quality standards, which include the definition of field and TLS data processing protocols, for TLS data sets used for training and benchmarking of tree classification models enhancing the performance stability of developed tree species classification approaches and user's trust in them.

Conclusion

For the seven tree species considered (*Birch, Ash, Beech, Spruce, Pine, Douglas-fir, Oak*) our results indicate that features of tree crowns -particularly branches of second and higher order and branch arrangements- contribute most to the decisions of the models. This observation is particularly pronounced for *Birch, Beech, Spruce*, and *Oak*. For *Ash, Pine*, and *Douglas-fir*, stem segments contribute most for the decisions of the models. Under visual interpretation of saliency maps of *Spruce* and *Douglas-fir* it is observable that the models particularly focus on branches attached to the stems. For *Ash* the models focus on average in 64.4 % of the side-view projections on bends in tree stems. Since bent tree stems are not a trait exclusive to *Ash* our results may hint towards an issue with the used data set in which bent stems are predominantly a feature specific to *Ash*. This may result in poor ability of the models to generalize well on unseen data. The tested models regard similar tree species alike as a human expert would do when looking only at the habitus of trees. Our results should be interpreted as an indication of which tree features are most accessible to the models under the chosen study design. In this regard the presented approach highlights model limitations, potential biases (shortcut learning), and can be used to promote confidence in model predictions. Our results further highlight the need for researching how CNN models perform the task of tree species classification using TLS data in more depth than only reporting performance results to enhance the quality of data sets used for development and benchmarking of classification models, which can benefit the performance and stability of classification models.

Funding

The research leading to these results has received funding from the European Union Horizon Europe Research & Innovation programme under the Grant Agreement no. 101056907 (PathFinder). Further it was part of the Center for Research-based Innovation SmartForest: Bringing Industry 4.0 to the Norwegian forest sector (NFR SFI project no. 309671, smartforest.no).

Conflict of interest statement

None declared.

Data availability statement

The data underlying this article are available in the FOR-species20K data set repository, at <https://doi.org/10.5281/zenodo.13255197>

Author contributions

Adrian Straker developed the ideas, designed the methodology, performed the data analysis, and led the manuscript writing. Marco Zullich provided substantial knowledge in the field of XAI and contributed the section *Finer-CAM description*. Nils Nölke and Paul Magdon supported the development of the research design. Johannes Breidenbach supported in the interpretation of the results. Max Freudenberg developed the side-view projection approach. Christoph Kleinn supported the statistical analysis. Stefano Puliti supported the dataset compilation. All authors contributed critically to the drafts.

References

Allen MJ *et al.* Tree species classification from complex laser scanning data in Mediterranean forests using deep learning. *Methods in Ecology and Evolution* 2023;14(7);1657-67.
<https://doi.org/10.1111/2041-210X.13981>.

Bender R, Lange S. Adjusting for multiple testing--when and how? *J Clin Epidemiol.* 2001;54(4);343-9.
[https://doi.org/10.1016/s0895-4356\(00\)00314-0](https://doi.org/10.1016/s0895-4356(00)00314-0).

Bertrand A *et al.* How cognitive biases affect XAI-assisted decision-making: A systematic review. *Proceedings of the 2022 AAAI/ACM Conference on AI, Ethics, and Society* 2022;78-91.
<https://doi.org/10.1145/3514094.3534164>.

Bradski, G. 2000 The OpenCV Library. *Dr. Dobbs Journal of Software Tools*

Chattpadhyay A *et al.* Grad-cam++: Generalized gradient-based visual explanations for deep convolutional networks. *IEEE winter conference on applications of computer vision (WACV)* 2018;839-47. <https://doi.org/10.1109/WACV.2018.00097>.

Chen J, Chen Y, Liu Z. Classification of typical tree species in laser point cloud based on deep learning. *Remote Sensing* 2021;13(23);4750. <https://doi.org/10.3390/rs13234750>.

Elfwing *et al.* Sigmoid-weighted linear units for neural network function approximation in reinforcement learning, *Neural Networks* 2018;107;3-11.
<https://doi.org/10.1016/j.neunet.2017.12.012>.

Geirhos R *et al.* Shortcut learning in deep neural networks. *Nature Machine Intelligence* 2020;2(11);665–73. <https://doi.org/10.1038/s42256-020-00257-z>.

Gildenblatt J *et al.* PyTorch library for CAM methods. <https://github.com/jacobgil/pytorch-grad-cam> (25 Februar 2025, date last assessed).

Han T, Sánchez-Azofeifa GA. A Deep Learning Time Series Approach for Leaf and Wood Classification from Terrestrial LiDAR Point Clouds. *Remote Sensing* 2022;14(13);3157.
<https://doi.org/10.3390/rs14133157>.

Heravi E J *et al.* An optimized convolutional neural network with bottleneck and spatial pyramid pooling layers for classification of foods 2018;105;50-8.
<https://doi.org/10.1016/j.patrec.2017.12.007>.

Hinns J, Martens D. Aggregating Local Saliency Maps for Semi-Global Explainable Image Classification. *ArXiv* 2025. <https://doi.org/10.48550/arXiv.2506.23247>.

Hinton *et al.* Improving neural networks by preventing co-adaptation of feature detectors. *ArXiv* 2012. <https://doi.org/10.48550/arXiv.1207.0580>.

Ioffe S, Szegedy C. Batch Normalization: Accelerating Deep Network Training by Reducing Internal Covariate Shift. *Proceedings of the 32nd International Conference on Machine Learning* 2015; **37**: 448 – 56.

Jocher G, Qiu J, Chaurasia A. *Ultralytics YOLO (Version 8.0.0) [Computer software]*. <https://github.com/ultralytics/ultralytics> (25 Februar 2025, date last assessed).

Kim TK *et al.* Identifying and extracting bark key features of 42 tree species using convolutional neural networks and class activation mapping. *Scientific Reports* 2022; **12**(1):4772. <https://doi.org/10.1038/s41598-022-08571-9>.

Lapuschkin S *et al.* Unmasking CleverHans predictors and assessing what machines really learn. *Nature communications* 2019; **10**(1):1096. <https://doi.org/10.1038/s41467-019-08987-4>.

Lin H *et al.* Identification of Tree Species in Forest Communities at Different Altitudes Based on Multi-Source Aerial Remote Sensing Data. *Applied Sciences* 2023; **13**(8):4911. <https://doi.org/10.3390/app13084911>.

Lines ER *et al.* AI applications in forest monitoring need remote sensing benchmark data sets. 2022 *IEEE International Conference on Big Data (Big Data)* 2022;4528-33. <https://doi.org/10.1109/BigData55660.2022.10020772>

Liu M *et al.* Tree species classification of LiDAR data based on 3D deep learning. *Measurement* 2021; **177**:109301. <https://doi.org/10.1016/j.measurement.2021.109301>.

Liu B *et al.* Individual tree species classification using the pointwise MLP-based point cloud deep learning method. *Environmental Sciences Proceedings* 2022; **22**(1):19. <https://doi.org/10.3390/IEc2f022-13049>.

Onishi M, Ise T. Explainable identification and mapping of trees using UAV RGB image and deep learning. *Scientific reports* 2021; **11**(1):903. <https://doi.org/10.1038/s41598-020-79653-9>.

Otsu N. A threshold selection method from gray-level histograms. *Automatica* 1975; **11**(285-296):23-7. <https://doi.org/10.1109/TSMC.1979.4310076>.

Ma Y *et al.* A deep-learning-based tree species classification for natural secondary forests using unmanned aerial vehicle hyperspectral images and LiDAR. *Ecological Indicators* 2024; **159**:111608. <https://doi.org/10.1016/j.ecolind.2024.111608>.

Marvasti-Zadeh SM *et al.* Crown-CAM: Interpretable visual explanations for tree crown detection in aerial images. *IEEE Geoscience and Remote Sensing Letters* 2023; **20**:1-5. <https://doi.org/10.1109/LGRS.2023.3271649>.

Mizoguchi T *et al.* Lidar-based individual tree species classification using convolutional neural network. In *Videometrics, range imaging, and applications XIV* 2017; **10332**; 193-9. <https://doi.org/10.1117/12.2270123>.

Mohseni S, Zarei N, Ragan ED. A multidisciplinary survey and framework for design and evaluation of explainable AI systems. *ACM Transactions on Interactive Intelligent Systems (TiiS)* 2021; **11(3-4)**; 1-45. <https://doi.org/10.1145/3387166>.

Molnar C. *Interpretable Machine Learning*, 3 edition, ISBN 978-3-911578-03-5

Muhammad MB, Mohammed B, Mohammed Y. Eigen-cam: Class activation map using principal components. *2020 International Joint Conference on Neural Networks (IJCNN)*, Glasgow, UK 2020; 1-7. <https://doi.org/10.1109/IJCNN48605.2020.9206626>.

Puliti S *et al.* Benchmarking tree species classification from proximally-sensed laser scanning data: introducing the FOR-species20K data set. *Methods in Ecology and Evolution* 2025; **16(4)**; 801-18. <https://doi.org/10.1111/2041-210X.14503>.

Riley RD, Collins GS. Stability of clinical prediction models developed using statistical or machine learning methods. *Biometrical Journal*. 2023; **65(8)**; 2200302. <https://doi.org/10.1002/bimj.202200302>.

Seidel D *et al.* Predicting tree species from 3D laser scanning point clouds using deep learning. *Frontiers in Plant Science* 2021; **12**. <https://doi.org/10.3389/fpls.2021.635440>.

Selvaraju RR *et al.* 2020 Grad-CAM: Visual Explanations from Deep Networks via Gradient-Based Localization. *International Journal of Computer Vision* 2020; **128**; 336-59. <https://doi.org/10.1007/s11263-019-01228-7>.

Smith LN, Topin N. Super-convergence: Very fast training of neural networks using large learning rates. *Artificial intelligence and machine learning for multi-domain operations applications* 2019; **11006**; 369-86. <https://doi.org/10.1117/12.2520589>.

Sun Z *et al.* YOLO-ITC: A New YOLO Method for Instance Segmentation of Individual Tree Crowns. *IEEE Transactions on Emerging Topics in Computational Intelligence* 2025. <https://doi.org/10.1109/TETCI.2025.3543833>.

Suzuki S, Abe K. 1985 Topological structural analysis of digitized binary images by border following. *Computer vision, graphics, and image processing* 1985; **30(1)**; 32-46. [https://doi.org/10.1016/0734-189X\(85\)90016-7](https://doi.org/10.1016/0734-189X(85)90016-7).

Straker A *et al.* 2023 Instance segmentation of individual tree crowns with YOLOv5: A comparison of approaches using the ForInstance benchmark LiDAR data set. *ISPRS Open Journal of Photogrammetry and Remote Sensing* 2023; **9**; 100045. <https://doi.org/10.1016/j.phphoto.2023.100045>.

Lin TY *et al.* 2014 Microsoft coco: Common objects in context. *Computer Vision – ECCV 2014. ECCV 2014. Lecture Notes in Computer Science* 2014; **8693**; 740-55. https://doi.org/10.1007/978-3-319-10602-1_48.

Liu B *et al.* Tree species classification using ground-based LiDAR data by various point cloud deep learning methods. *Remote Sensing* 2022;14(22):5733. <https://doi.org/10.3390/rs14225733>.

Lines ER *et al.* AI applications in forest monitoring need remote sensing benchmark datasets. *IEEE international conference on big data (big data)* 2022; 4528-33.
<https://doi.org/10.1109/BigData55660.2022.10020772>.

van der Walt S *et al.* scikit-image: image processing in Python. *PeerJ* 2:e453 2014.
<https://doi.org/10.7717/peerj.453>.

Xi Z *et al.* See the forest and the trees: Effective machine and deep learning algorithms for wood filtering and tree species classification from terrestrial laser scanning. *ISPRS Journal of Photogrammetry and Remote Sensing* 2020;168:1-16.
<https://doi.org/10.1016/j.isprsjprs.2020.08.001>.

Zhang Z *et al.* Finer-cam: Spotting the difference reveals finer details for visual explanation. *Proceedings of the IEEE/CVF Conference on Computer Vision and Pattern Recognition (CVPR)* 2025;9611-20.

Zhou B *et al.* Learning deep features for discriminative localization. *Proceedings of the IEEE Conference on Computer Vision and Pattern Recognition (CVPR)* 2016;2921-29.

Zou X *et al.* Tree classification in complex forest point clouds based on deep learning. *IEEE Geoscience and Remote Sensing Letters* 2017;14(12):2360-2364.
<https://doi.org/10.1109/LGRS.2017.2764938>.

Appendix

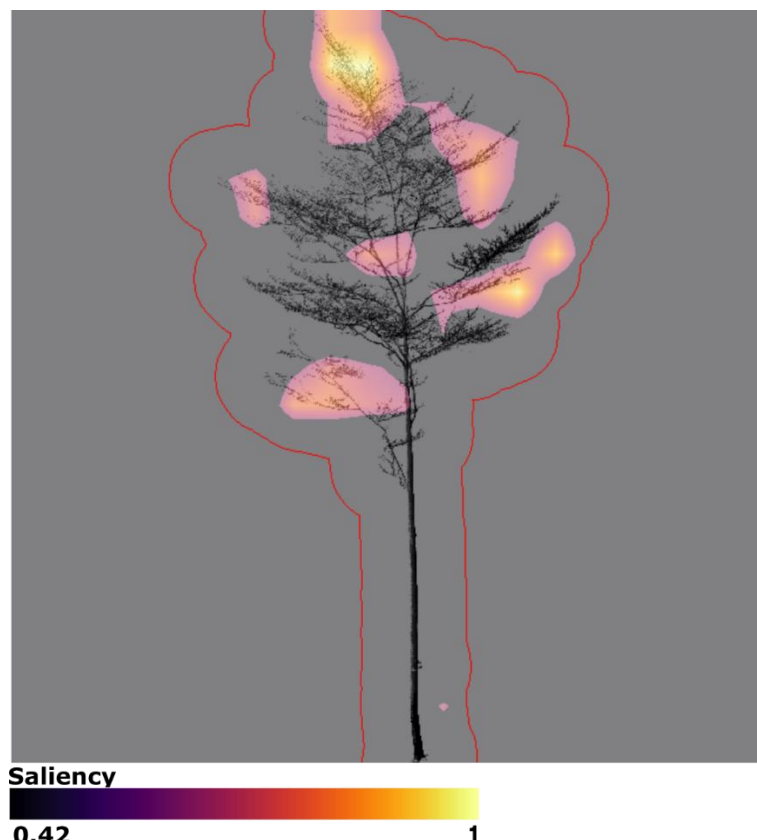


Figure I Saliency map of Beech overlayed with its respective TLS side-view showing only salient pixel above a threshold (0.42) defined by the application of Otsu's method. Layer activations for a species class are depicted in a colour gradient from purple to yellow, where yellow and purple correspond to the regions with high and low importance attached to them, respectively. Red outline depicts the tree segment contour.

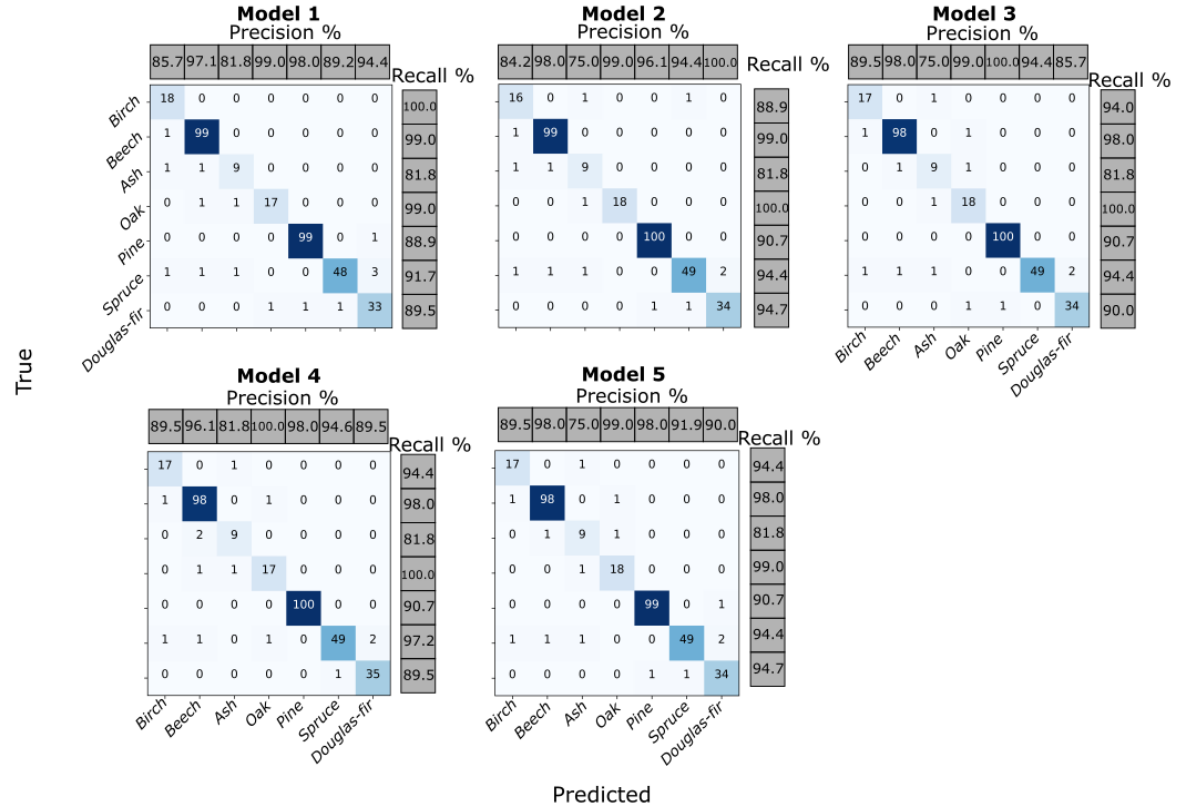


Figure II: Confusion matrices, class-wise precisions and recalls of all five trained YOLOv8 models applied to the test data set.

Table a: Species-wise analysis results of the ratios of the number of salient pixels associated to the image segments in % (standard deviation in brackets) of each trained YOLOv8 model.

Tree species	Model No.	Crown	Stem	Crown top	Crown middle	Crown base	Crown edge buffer
<i>Birch</i>	1	79.8 (23.5)	20.2 (23.5)	19.2 (18.5)	32.7 (21.9)	48.07 (22.2)	56.2 (17.9)
	2	70.9 (22.8)	29.1 (22.8)	12.0 (18.4)	26.1 (16.5)	61.9 (20.3)	63.4 (17.4)
	3	80.9 (17.3)	19.1 (17.3)	13.1 (14.1)	32.9 (19.0)	54.0 (21.6)	69.4 (11.5)
	4	81.5 (24.5)	18.5 (24.5)	21.2 (24.4)	36.0 (20.3)	42.7 (26.9)	48.9 (11.9)
	5	77.7 (23.7)	22.3 (23.7)	17.0 (24.0)	31.4 (21.2)	51.5 (24.1)	54.8 (15.9)
<i>Beech</i>	1	84.6 (23.3)	15.4 (23.3)	38.5 (16.5)	36.7 (13.2)	24.8 (18.8)	59.0 (18.2)
	2	85.7 (19.5)	14.3 (19.5)	36.7 (16.4)	35.6 (13.9)	27.7 (14.9)	61.8 (16.5)
	3	84.2 (21.5)	15.8 (21.5)	41.9 (16.2)	32.2 (8.9)	26.0 (15.3)	54.4 (22.3)
	4	84.7 (20.4)	15.3 (20.4)	44.3 (15.3)	33.9 (15.6)	21.8 (12.9)	60.4 (13.0)
	5	86.8 (19.9)	13.2 (19.9)	44.8 (17.7)	33.9 (12.7)	21.4 (14.4)	60.5 (22.0)
<i>Ash</i>	1	53.4 (31.7)	46.6 (31.7)	21.2 (19.9)	46.5 (26.0)	32.3 (30.4)	54.2 (26.9)
	2	43.3 (27.6)	56.7 (27.6)	26.2 (26.7)	23.6 (20.8)	50.2 (39.0)	57.3 (34.3)
	3	54.6 (26.6)	45.4 (26.6)	38.4 (29.6)	34.6 (23.7)	27.0 (28.2)	41.7 (33.2)
	4	54.2 (26.9)	45.8 (26.9)	39.6 (32.0)	22.1 (16.5)	38.3 (33.4)	57.2 (19.5)
	5	57.0 (19.5)	43.0 (19.5)	32.9 (21.8)	33.5 (17.1)	33.6 (26.8)	52.7 (27.2)
<i>Spruce</i>	1	84.0 (32.7)	16.0 (32.7)	37.5 (23.9)	43.6 (20.0)	18.9 (20.6)	42.3 (24.2)
	2	78.6 (30.9)	21.4 (30.9)	23.1 (11.9)	44.6 (16.8)	27.3 (15.9)	29.6 (20.1)
	3	72.9 (38.0)	27.1 (38.0)	15.4 (16.7)	46.0 (22.6)	28.6 (23.1)	27.1 (18.9)
	4	84.8 (24.9)	15.2 (24.9)	26.0 (17.3)	50.1 (14.9)	23.9 (17.8)	32.6 (16.2)
	5	68.2 (37.7)	31.8 (37.7)	14.6 (16.6)	40.3 (24.1)	35.2 (30.0)	36.1 (23.1)
<i>Pine</i>	1	43.3 (25.2)	56.7 (25.2)	17.6 (17.4)	38.3 (18.0)	44.1 (32.0)	49.7 (22.6)
	2	33.5 (27.7)	66.5 (27.7)	14.3 (21.7)	31.6 (23.4)	44.0 (35.4)	44.6 (27.6)
	3	41.6 (28.1)	58.4 (28.1)	20.8 (19.3)	40.8 (18.9)	38.4 (31.7)	58.0 (24.2)
	4	41.5 (25.6)	58.5 (25.6)	22.9 (23.0)	42.4 (21.5)	34.8 (29.0)	50.3 (25.2)
	5	39.8 (26.9)	60.2 (26.9)	23.3 (23.8)	42.6 (23.3)	34.1 (29.6)	40.9 (24.7)
<i>Douglas-fir</i>	1	48.3 (36.3)	51.7 (36.3)	5.8 (10.8)	26.4 (26.1)	62.8 (33.3)	40.9 (29.2)
	2	62.1 (30.3)	37.9 (30.3)	7.8 (12.3)	34.1 (24.9)	58.0 (28.0)	44.7 (20.7)
	3	61.1 (26.6)	38.9 (26.6)	17.6 (20.2)	40.2 (27.0)	42.2 (32.7)	31.6 (23.6)
	4	51.3 (38.0)	48.7 (38.0)	22.3 (31.7)	32.9 (30.3)	39.7 (35.3)	38.1 (31.6)
	5	61.6 (28.3)	38.4 (28.3)	17.6 (19.4)	38.7 (26.2)	43.7 (31.4)	41.6 (20.8)
<i>Oak</i>	1	82.4 (24.1)	17.6 (24.1)	23.1 (16.6)	38.3 (13.1)	38.6 (22.0)	41.0 (20.8)
	2	85.2 (21.0)	14.8 (21.0)	34.0 (21.3)	34.4 (14.8)	31.6 (20.5)	44.4 (20.6)
	3	83.8 (20.5)	16.2 (20.5)	30.0 (17.4)	29.1 (17.4)	40.9 (25.1)	44.5 (20.7)
	4	80.7 (30.0)	19.3 (30.0)	22.0 (16.3)	37.6 (17.8)	34.8 (22.9)	39.7 (24.0)
	5	88.9 (13.6)	11.1 (13.6)	22.9 (20.5)	40.1 (17.1)	37.0 (24.0)	51.8 (18.6)